Petroleum Science
https://doi.org/10.1007/s12182-020-00428-y

ORIGINAL PAPER

Thermally enhanced shale gas recovery: microstructure characteristics of combusted shale

Yuan-Hao Cao[1] · Wei Chen[1] · Teng-Xi Wang[2] · Yin-Nan Yuan[1]

Received: 21 August 2019

Abstract
Recently, thermal recovery technologies such as combustion have been studied for shale gas recovery. Thus, understanding of the microstructure of combusted shale is essential for evaluating the effects of thermal treatment on shale gas transport capacity. In this study, the effect of combustion on shale microstructure changes was investigated. Firstly, different-sized shale samples were combusted at 450 °C for 30 min. Afterward, shale microstructure properties including surface topographies, porosity and permeability of the raw and combusted shale samples were measured and compared. It was found that the pore volume and specific surface area increased after combustion, especially for small pulverized samples. According to surface topography obtained from atomic force microscope, more rough surfaces were obtained for the combusted shale due to larger pores and generation of thermal fractures caused by the removal of organic matter. Based on the mercury intrusion porosimetry measurements, the porosity of the shale samples increased from 2.79% to 5.32% after combustion. In addition, the permeability was greatly improved from 0.0019 to 0.6759 mD, with the effective tortuosity decreased from 1075.40 to 49.27. As a result, combustion treatment can significantly improve the gas transport capacity.

Keywords Shale · Combustion · Microstructure · Porosity · Permeability · Particle size

1 Introduction

Because of abundant reserves and low carbon emissions of shale gas, extraction of hydrocarbon products from shale reservoirs has attracted worldwide interests (Chen et al. 2017a; Huang and Zhao 2017). However, shale has extremely low permeability and complicated pore system, which is characterized by various pore types and wide pore size distributions (Sarkar et al. 2018). These characteristics significantly affect gas storage and flow transport behavior (Bai et al. 2019; Chen et al. 2016; Deng et al. 2016; Ji et al. 2016; Tian et al. 2013). Hence, a large-scale extraction of the shale gas from the tight shale matrix is challenging. Recently, the combustion treatment has been proposed for shale gas recovery (Chapiro and Bruining 2015; Chen et al. 2017b). Combustion treatment not only provides energy for gas desorption from pore surfaces but also promotes the gas transport by improving the permeability (Chen et al. 2017b, 2018a, 2019c, d). However, pore system evolution during combustion process involves complicated physical and chemical processes. The knowledge in this area is still limited and needs further exploration.

Various classifications of pore types in shale have been proposed in previous studies (Desbois et al. 2009; Heath et al. 2011; Loucks et al. 2012; Pommer and Milliken 2015; Slatt and O'Brien 2011; Zhu et al. 2018). Based on pore size, shale pores could be divided into three types: micropore (< 2 nm), mesopore (2–50 nm) and macropore (> 50 nm) (Sing et al. 1985). Nanoscale gas transport mechanism and gas adsorption capacity in shale vary with different pore sizes and structures (Yu et al. 2017). The enlarged nanopores can lead to an increase in the conductivity of slippage flow and the contribution degree of slippage flow to the total gas transport capacity (Sun et al. 2019). In addition, the non-negligible gas adsorption and surface diffusion in the micropores and fine mesopores (< 10 nm) significantly affect the potential of the storage and transport of shale gas (Xiong

Edited by Yan-Hua Sun

✉ Wei Chen
timtamu@suda.edu.cn

[1] School of Energy, Soochow University, Suzhou 215006, Jiangsu, China

[2] Department of Mechanical Engineering, Texas A&M University, College Station 77840, USA

Published online: 20 February 2020

et al. 2017; Yu et al. 2017). Based on pore connectivity, shale pores can be divided into interparticle pores, intraparticle pores and organic pores (Katz and Arango

These analysis results are given in Table 1 (Chen et al. 2019d).

2.3 Pore characteristics of shale samples

In order to obtain pore characteristics of the shale samples, low-temperature N_2 adsorption measurements were performed using a Micromeritics TriStar II 3020 surface area analyzer. Before the measurements, all samples were dried and degassed at a constant temperature of 100 °C for 4 h to remove moisture and adsorbed gases. Then, about 0.2 g of these samples was analyzed exposed to N_2 at 77 K. The N_2 adsorption volume was measured with relative pressure (P/P_0) ranging from 0.050 to 0.995. The pore parameters such as pore volume, surface area and pore size distribution can be calculated using multiple adsorption theories such as Langmuir, Brunauer–Emmett–Teller (BET) and Barrett–Joyner–Halenda (BJH).

In this study, the raw and combusted samples with the particle size of 0.71–1.00 mm (RS1 and CS1) were sent to a commercial laboratory for the MIP test to measure the shale porosity and permeability. MIP tests were performed using a Micromeritics IV AutoPore 9500 Instrument, with the maximum pressure of 227.45 MPa. The shale samples RS1 and CS1 were dried and degassed prior to the tests. The porosity, permeability and effective tortuosity of the raw and combusted samples were investigated.

2.4 Morphology analyses of shale samples

The microstructure and morphology of the raw and combusted shale samples were analyzed using SEM and AFM imaging study. Before the experiments, in order to reduce the error of experimental results caused by heterogeneity of shale, the observation position was marked on the shale sample. The SEM equipment used (HITACHI SU8010) was operated under an acceleration voltage of 1 kV and a beam current of 10 μA. The scanning range of the AFM used (MFP-3D-BIO) was $90 \times 90 \times 15$ μm, with accuracy of 0.6 nm and height precision less than 0.03 nm.

3 Results and discussion

3.1 Shale properties

As shown in Table 1, the shale sample has a high ash content of 87.58%, and the total organic matter is around 10%, including 2.39% fixed carbon and 7.44% volatile matter. The high content of organic matter provides a large amount of potential adsorption sites for shale gas (Chen et al. 2018a). According to the kerogen-type descriptions, the kerogen type of these shale samples is dominated by Type II with the H/C atomic ratios about 1.07 and O/C atomic ratios about 0.145 (Jarvie 2015). The vitrinite reflectance (R_o) is 2.7%, which shows a relatively high thermal maturity, indicating that the shale was in the dry gas window (Jarvie 2015), while for high mature shale ($R_o = 2.7\%$) the amount of the dissolved gas would be ignored (Guo 2013).

Table 1 Proximate analysis, ultimate analysis and vitrinite reflectance of shale sample, adapted from Chen et al. (2019d)

Moisture, %	Ash, %	Volatile matter, %	Fixed carbon, %	Carbon, %	Oxygen, %	Hydrogen, %	Nitrogen, %	Sulfur, %	Vitrinite reflectance R_o, %
2.59	87.58	7.44	2.39	5.36	1.04	0.48	0.26	5.36	2.7

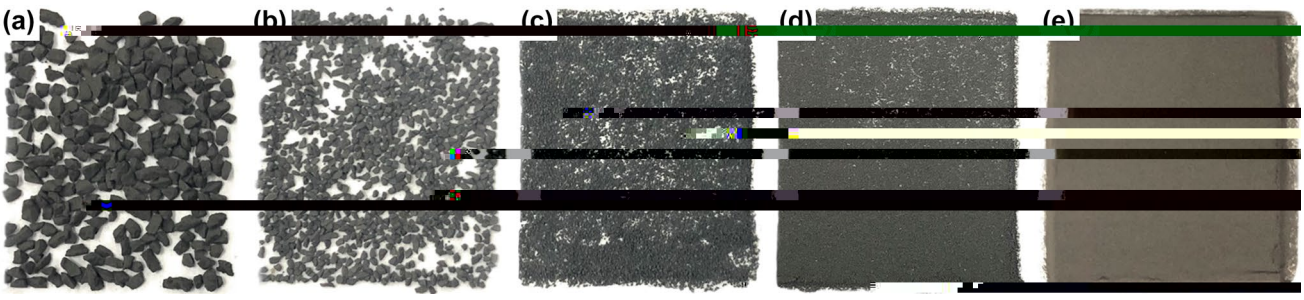

Fig. 1 Combusted shale samples with different particle sizes: **a** 0.710–1.000 mm, **b** 0.355–0.450 mm, **c** 0.088–0.150 mm, **d** 0.045–0.063 mm, **e** 0–0.045 mm

3.2 Low-temperature N_2 adsorption m reme

3.2.1 N_2 adsorption–desorption isotherms

According to IUPAC, six sorption isother o VI) four types of hysteresis loops (H1 to H4) are nonly to characterize the sorption behavior of p mate (Sing et al. 1985). Figure 2 shows the N_2 tion- orption isotherms of the shale samples. Alt not s ing a plateau at high P/P_0, these isotherm ll si to the IUPAC type IV isotherms, indicati pres of mesopores and macropores (Sing et al. Tian 2013). The hysteresis loops of these isotl all c spond to type H4, which are often associa th n slit-shaped pores (Liu et al. 2018; Lowell 004 et al. 1985). It was found that the slit po ictu a higher gas transport capacity than other stru such as circular pores (Yu et al. 2019). Th of c of the hysteresis loops at low relative pres an a found in previous studies (Chen et al. 2015 o; M erz et al. 2012), thought to be associated wit wel the porous structure or the irreversible upta mol in pores (Sing et al. 1985).

The sample RS1 shown in Fig. 2a with t ges cle size adsorbed the least amount of N_2 (0. ^{3}/g) the sample RS5 with the smallest particle s d th est adsorption volume (14.35 cm^3/g). Th ds capacity of the samples increased with th as particle size, indicating that the pulverizat ake pores accessible.

It is shown in Fig. 2b that the isotherm hy loops of the combusted shale samples we la samples. The amounts of adsorbed N_2 inc fr

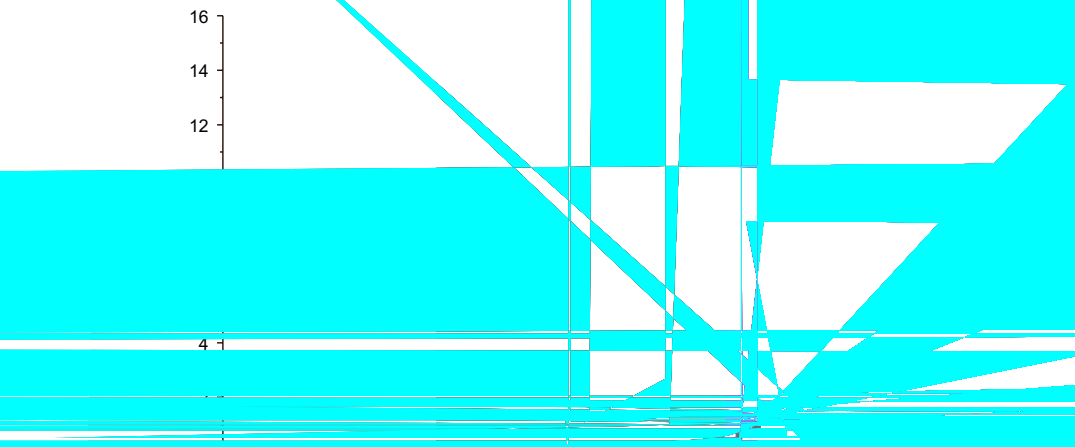

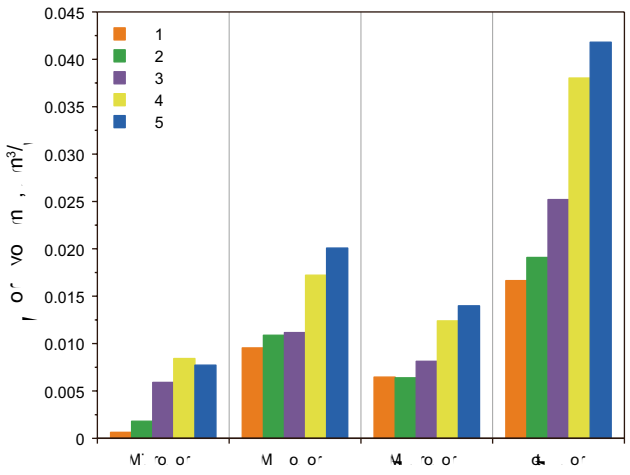

Fig. 3 The volumes of micropores, mesopores, macropores and the total pores of the different-sized combusted samples based on *t*-plot method and BJH method

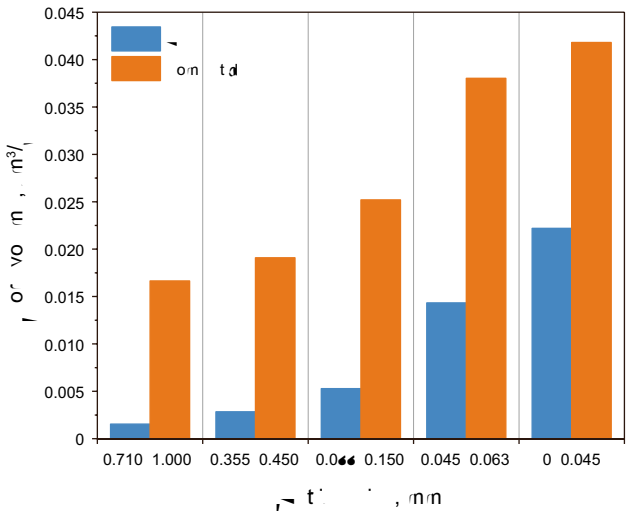

Fig. 4 The pore volumes of different-sized particles of raw and combusted shale samples based on *t*-plot method and BJH model

1.54×10^{-3} cm^3/g (RS1) to 22.19×10^{-3} cm^3/g (RS5). The increased pore volume of 20.65×10^{-3} cm^3/g showed the volume of newly exposed pores. It was 4.5×10^{-3} cm^3/g less than the amount in combusted samples. Moreover, raw sample of each size had much smaller pore volume than the combusted samples. This can be attributed to the combustion treatment which can further improve the porosity and pore connectivity of shale. Compared with pulverization, the combustion treatment can significantly improve the porosity of shale. It is interesting that the increased pore volumes after combustion were all around 20×10^{-3} cm^3/g, which may reflect the amount of removed organic matter. This indicates that the effect of combustion on shale pores is mainly reflected in the removal of organic matter and the enlargement of organic pores.

3.2.3 Pore surface area

The surface area plays a key role in the adsorption of the shale gas. The change tendency of pore surface areas was similar to that of pore volume. The specific surface areas measured based on the BET method are given in Fig. 5. The specific surface areas of the combusted samples increased from 8.99 m^2/g (CS1) to 27.91 m^2/g (CS5) with decreasing particle size, while those of the raw samples from 0.4199 m^2/g (RS1) to 6.5886 m^2/g (RS5). The surface areas of raw and combusted samples all increased with the decrease in particle size because of the newly developed open pores by pulverization. It also can be seen that the specific surface areas significantly increased after combustion. Given that the specific surface area is mainly affected by smaller pores (Tian et al. 2013) and the micropores in shale are largely developed in organic matter (Li et al. 2016), the increase in specific surface area may be mainly attributed to the oxidization of organic matter by combustion. In the oxidization process, numerous small organic pores enlarged, respectively. However, there are also some studies that found that the specific surface areas of shale decreased after combustion. This may be due to the differences in sample properties and the oxidation degree of organic matter in shale.

3.2.4 Pore size distribution

The pore size distributions of raw and combusted shale samples were analyzed using BJH adsorption data and are given

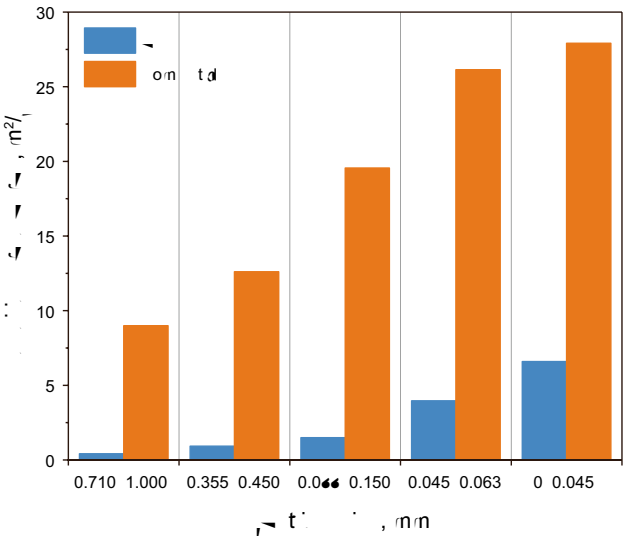

Fig. 5 The specific surface areas of shale samples based on BET method

in Fig. 6. After combustion, the pore volumes of micropores, mesopores and macropores were all increased, which means more flow transport channels were created. For high mature shale, micropores are well developed and hosted in organic matter (Tian et al. 2013; Yang et al. 2016). Under high-temperature combustion, a large amount of original closed micropores were reopened and the organic matters were decomposed, both of which resulted in the generation of significant micropores. The original stored gases in the closed pores became extractable. Besides, more mesopores and macropores were obtained due to the oxidization of organic matter. In micropores and mesopores, the gas flow was mainly slip flow or free molecular diffusion flow. As the pore size increased (Knudsen number *Kn* decreases), the gas transport shifted from diffusion flow to slip flow (Sun et al. 2019; Darabi et al. 2012). Thus, the gas transport capacity was improved.

3.3 The porosity and permeability of combusted shale

The porosity and permeability are the most important parameters to assess the gas transport in shale. Based on the results from MIP tests, it was found that the porosity of shale increased sharply from 2.79% to 5.32% after combustion at 450 °C. Furthermore, the permeability was greatly improved from 0.0019 to 0.6759 mD, with the effective tortuosity decreased from 1075.40 to 49.27.

Combustion resulted in not only the enlargement of open pores but also the generation of microfractures and the exposure of inaccessible pores. In addition, the decrease in effective tortuosity can also improve gas diffusion capacity. The diffusion coefficient can be given as (Veltzke and Thöming 2012):

$$D_{\mathrm{k}} = \frac{1}{3} s \sqrt{\frac{8RT}{\pi M}} \tag{1}$$

where s is the pore diameter and M is molar mass.

The effective tortuosity τ is often related to effective diffusion coefficient (Sun et al. 2018):

$$\tau = \frac{D_{\mathrm{k}}}{D_{\mathrm{e}}} = \frac{1}{\phi}\left(\frac{L_{\mathrm{e}}}{L}\right)^2 \tag{2}$$

where D_{e} is the effective diffusion coefficient in the porous media, m^2/s; ϕ is porosity, and L_{e}/L is the geometrical tortuosity.

Thus, the significant decrease in effective tortuosity τ indicates the improvement in effective diffusion coefficient based on Eqs. (1) and (2). This reveals that the gas diffusion potential inside shale pore systems was promoted after combustion treatment.

3.4 Pore-fracture morphology analyses based on SEM images

In order to study the microstructures of shale, the pore-fracture morphologies of the raw and combusted shale samples were observed using SEM. It is shown in Fig. 7a that the open pore networks in these samples mainly consisted of interparticle pores connected by microfractures. Numerous flocculated clay microfabrics are also shown in Fig. 7b, d. As a result of thermal cracking, the obvious microfractures that existed in combusted shale samples (Fig. 7c, d) can significantly improve the porosity and permeability of shale.

During the pulverization process, many closed pores were exposed to microfractures and the isolated intraparticle pores, such as pores in Fig. 7a, might be enlarged. In

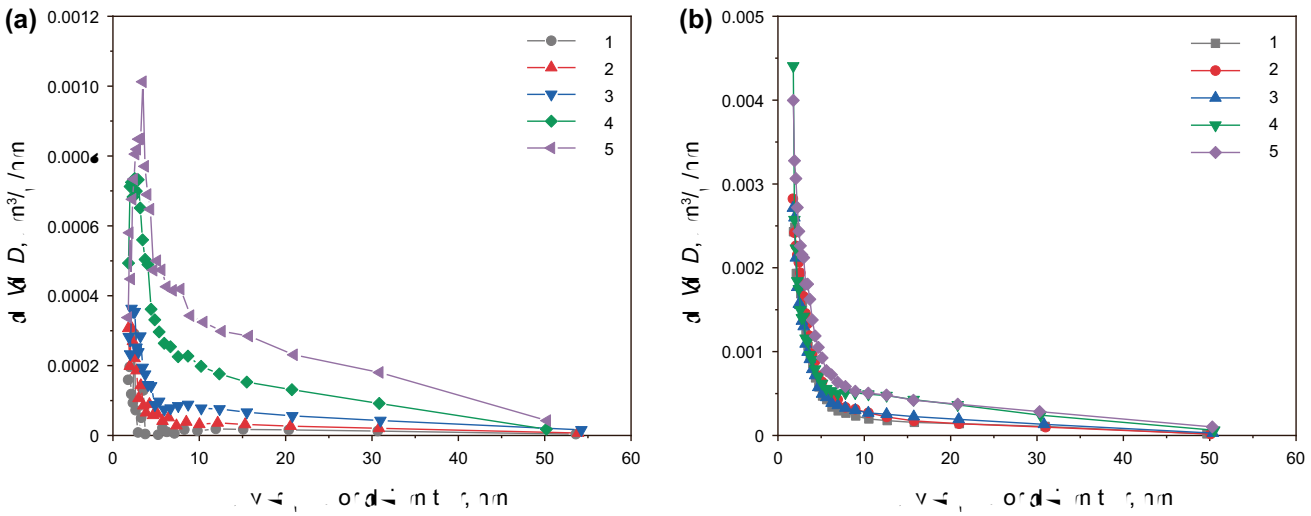

Fig. 6 Pore size distribution of (**a**) raw and (**b**) combusted shale samples from BJH adsorption data

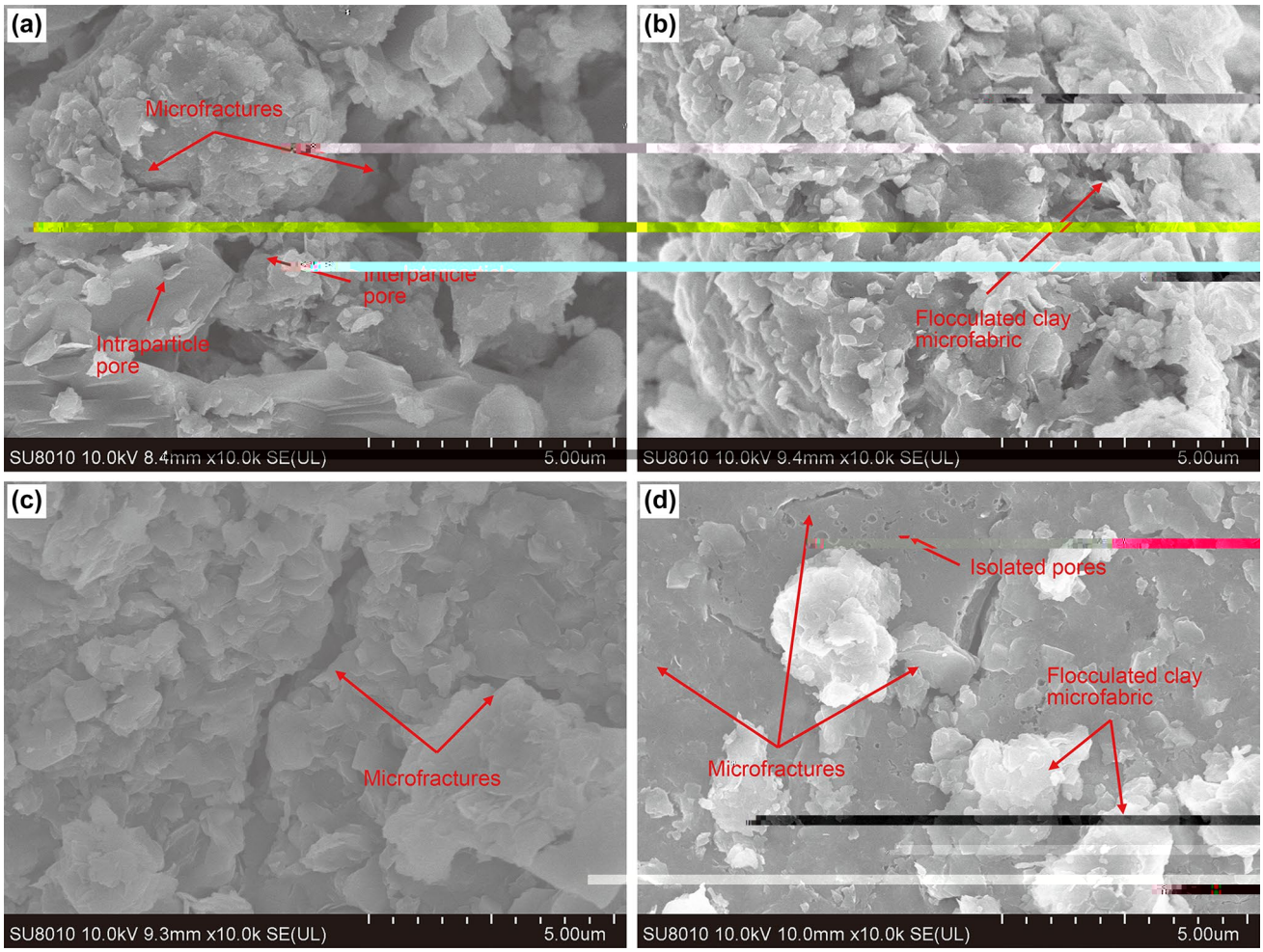

Fig. 7 SEM images of (**a**, **b**) raw and (**c**, **d**) combusted shale samples

addition, the microfractures were possibly generated. The original open pore networks could be developed due to the newly developed microfractures. This process reflects the enhancement of the pore connectivity.

3.5 AFM topography image of shale sample

During the combustion, some kerogen on the shale surface was removed and released as gas through oxidization (Chen et al. 2017b). To investigate the changes in shale morphology at the beginning of the rapid oxidization stage, the shale sample (RS1) was combusted at 400 °C for 30 min. The surface topographies of the shale samples before and after combustion (400 °C) were investigated using AFM. Using a sharp probe (a few nanometers in diameter) to measure the forces between the probe and the sample as a function of their mutual distance, nanoscale surface topography of shale surface (2D and 3D) was obtained, as shown in Fig. 8. The grooves (darker areas) in the grayscale images can be considered as nanopores (Javadpour and Ettehadtavakkol 2015). The raw shale sample (Fig. 8a, b) had more even surfaces with about 1.4 μm in height and the maximum depth of 1.2 μm, while the combusted shale sample (Fig. 8c, d) had a more uneven surface with about 2.4 μm in height and 2.0 μm in depth, indicating deeper groove areas. This indicates that more organic matter was removed from the shale and resulted in larger pore volume. Moreover, the inaccessible pores blocked or restricted by organic matter might be connected to pore networks after combustion treatment.

It can be seen from Fig. 9a that the surface depth of raw shale is mainly between 0.5 and 1.5 μm. Moreover, the depth around 1.2 μm has the biggest percentage. After being combusted at 400 °C, the shale got wider surface depth distribution, ranging from 0.3 to 3.2 μm (Fig. 9b). Deeper surfaces were produced and were mainly in the range of 1.5 to 3.2 μm. As discussed before, the removal of organic matter resulted in bigger pore depth and areas. In other words, the porosity of the shale samples could be improved.

4 Conclusions

In this study, the effects of combustion treatment on shale physical and geochemical proprieties such as porosity and permeability changes were investigated. The main conclusions are listed as follows:

(1) The total organic matter content of the shale sample is around 10%, and the vitrinite reflectance value (R_o) was 2.7%. The koise09((o(s).(etmeype shale sam)3(ple is)5( )TJ-. domi Tw23.478 0 TdTc-.0025 1w10 0 0 10 2).6(rna).5(b()TJy T

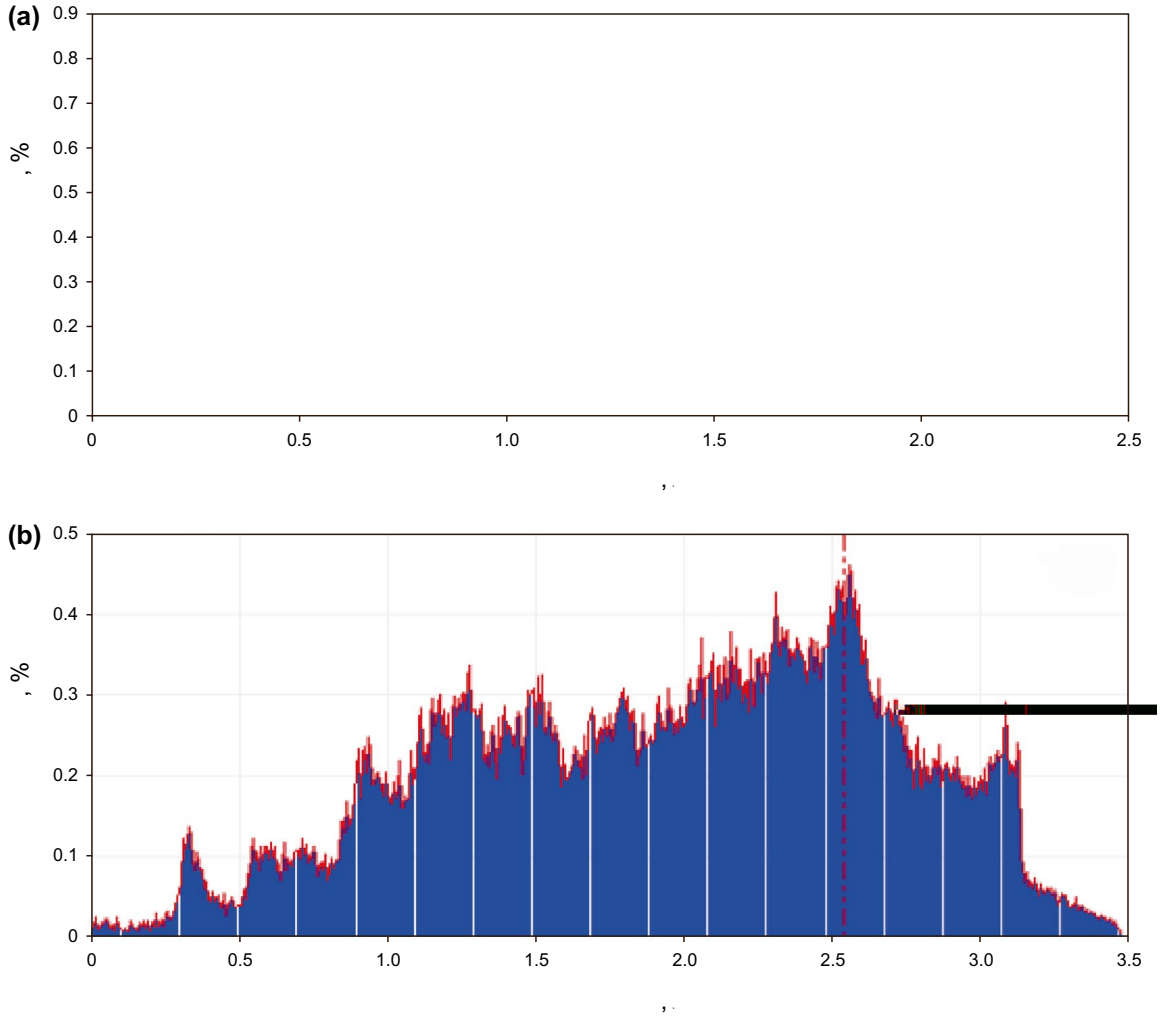

Fig. 9 Depth histogram of (**a**) raw and (**b**) combusted shale samples

Acknowledgements The authors wish to acknowledge the financial support from the National Natural Science Foundation of China (Grant No. 51776132) and the Natural Science Foundation of Jiangsu Province (Grant No. BK20181170).

References

Bai J, Kang Y, Chen M, Liang L, You L, Li X. Investigation of multi-gas transport behavior in shales via a pressure pulse method. Chem Eng J. 2019;360:1667–77. https://doi.org/10.1016/j.cej.2018.10.197.

Chapiro G, Bruining J. Combustion enhance recovery of shale gas. J Pet Sci Eng. 2015;127:179–89. https://doi.org/10.1016/j.petrol.2015.01.036.

Chen Y, Wei L, Mastalerz M, Schimmelmann A. The effect of analytical particle size on gas adsorption porosimetry of shale. Int J Coal Geol. 2015;138:103–12. https://doi.org/10.1016/j.coal.2014.12.012.

Chen W, Lei Y, Chen Y, Sun J. Pyrolysis and combustion enhance recovery of gas for two china shale rocks. Energy Fuels. 2016;30(12):10298–305. https://doi.org/10.1021/acs.energyfuels.6b02274.

Chen L, Jiang Z, Liu K, Tan J, Gao F, Wang P. Pore structure characterization for organic-rich Lower Silurian shale in the Upper Yangtze Platform, South China: a possible mechanism for pore development. J Nat Gas Sci Eng. 2017a;46:1–15. https://doi.org/10.1016/j.jngse.2017.07.009.

Chen W, Lei Y, Ma L, Yang L. Experimental study of high temperature combustion for enhanced shale gas recovery. Energy Fuels. 2017b;31(9):10003–10. https://doi.org/10.1021/acs.energyfuels.7b00762.

Chen W, Zhou Y, Yang L, Zhao N, Lei Y. Experimental study of low-temperature combustion characteristics of shale rocks. Combust Flame. 2018a;194:285–95. https://doi.org/10.1016/j.combustflame.2018.04.033.

Chen Y, Qin Y, Wei C, Huang L, Shi Q, Wu C, et al. Porosity changes in progressively pulverized anthracite subsamples: implications for the study of closed pore distribution in coals. Fuel. 2018b;225:612–22. https://doi.org/10.1016/j.fuel.2018.03.164.

Chen F, Lu S, Ding X, Ju Y. Evaluation of the density and thickness of adsorbed methane in differently sized pores contributed by various components in a shale gas reservoir: a case study of the Longmaxi Shale in Southeast Chongqing, China. Chem Eng J. 2019a;367:123–38. https://doi.org/10.1016/j.cej.2019.02.105.

Chen W, Lei Y, Hua X. Flow transportation inside shale rocks at low-temperature combustion condition: a simple scaling law. Combust Flame. 2019b;199:114–21. https://doi.org/10.1016/j.combustflame.2018.10.022.

Chen W, Yang J, Chen Y, Lei Y, Sun J, Wang T. Flow transportation inside shale samples during low temperature combustion: the effect of desorption and pyrolysis. Fuel. 2019c;242:77–83. https://doi.org/10.1016/j.fuel.2018.12.110.

Chen W, Zhou Y, Yu W, Yang L. Experimental study of low-temperature shale combustion and pyrolysis under inert and noninert environments. SPE Prod Oper. 2019d. https://doi.org/10.2118/194507-PA **Preprint**.

Darabi H, Ettehad A, Javadpour F, Sepehrnoori K. Gas flow in ultra-tight shale strata. J Fluid Mech. 2012;710:641–58. https://doi.org/10.1017/jfm.2012.424.

Deng H, Hu X, Li HA, Luo B, Wang W. Improved pore-structure characterization in shale formations with FESEM technique. J Nat Gas Sci Eng. 2016;35:309–19. https://doi.org/10.1016/j.jngse.2016.08.063.

Desbois G, Urai JL, Kukla PA. Morphology of the pore space in claystones—evidence from BIB/FIB ion beam sectioning and cryo-SEM observations. eEarth. 2009;4(1):15–22.

Guo S. Experimental study on isothermal adsorption of methane gas on three shale samples from Upper Paleozoic strata of the Ordos Basin. J Pet Sci Eng. 2013;110:132–8. https://doi.org/10.1016/j.petrol.2013.08.048.

Guo H, Jia W, Peng P, Zeng J, He R. Evolution of organic matter and nanometer-scale pores in an artificially matured shale undergoing two distinct types of pyrolysis: a study of the Yanchang Shale with Type II kerogen. Org Geochem. 2017;105:56–66. https://doi.org/10.1016/j.orggeochem.2017.01.004.

Han X, Jiang X, Yu L, Cui Z. Change of pore structure of oil shale particles during combustion. Part 1. Evolution mechanism. Energy Fuels. 2006;20(6):2408–12. https://doi.org/10.1021/ef0603277.

Heath JE, Dewers TA, McPherson BJOL, Petrusak R, Chidsey TC, Rinehart AJ, et al. Pore networks in continental and marine mudstones: characteristics and controls on sealing behavior. Geosphere. 2011;7(2):429–54. https://doi.org/10.1130/ges00619.1.

Hu QH, Liu XG, Gao ZY, Liu SG, Zhou W, Hu WX. Pore structure and tracer migration behavior of typical American and Chinese shales. Pet Sci. 2015;12(4):651–63. https://doi.org/10.1007/s12182-015-0051-8.

Huang X, Zhao Y. Characterization of pore structure, gas adsorption, and spontaneous imbibition in shale gas reservoirs. J Pet Sci Eng. 2017;159:197–204. https://doi.org/10.1016/j.petrol.2017.09.010.

Jarvie DM. Geochemical assessment of unconventional shale gas resource systems. In: Rezaee R, editor. Fundamentals of gas shale reservoirs. 1st ed. New Jersey: Wiley; 2015. p. 47–69.

Javadpour F, Ettehadtavakkol A. Gas transport processes in shale. In: Rezaee R, editor. Fundamentals of gas shale reservoirs. 1st ed. New Jersey: Wiley; 2015. p. 245–66.

Ji W, Song Y, Jiang Z, Meng M, Liu Q, Chen L, et al. Fractal characteristics of nano-pores in the Lower Silurian Longmaxi shales from the Upper Yangtze Platform, south China. Mar Pet Geol. 2016;78:88–98. https://doi.org/10.1016/j.marpetgeo.2016.08.023.

Katz BJ, Arango I. Organic porosity: a geochemist's view of the current state of understanding. Org Geochem. 2018;123:1–16. https://doi.org/10.1016/j.orggeochem.2018.05.015.

Li T, Tian H, Chen J, Cheng L. Application of low pressure gas adsorption to the characterization of pore size distribution of shales: an example from Southeastern Chongqing area, China. J Nat Gas Geosci. 2016;1(3):221–30. https://doi.org/10.1016/j.jnggs.2016.07.001.

Li B, Zhuang X, Li J, Querol X, Font O, Moreno N. Enrichment and distribution of elements in the Late Permian coals from the Zhina Coalfield, Guizhou Province, Southwest China. Int J Coal Geol. 2017;171:111–29. https://doi.org/10.1016/j.coal.2017.01.003.

Liu K, Wang L, Ostadhassan M, Zou J, Bubach B, Rezaee R. Nanopore structure comparison between shale oil and shale gas: examples from the Bakken and Longmaxi Formations. Pet Sci. 2018;16(1):77–93. https://doi.org/10.1007/s12182-018-0277-3.

Loucks RG, Reed RM, Ruppel SC, Jarvie DM. Morphology, genesis, and distribution of nanometer-scale pores in siliceous mudstones of the Mississippian Barnett Shale. J Sediment Res. 2009;79(12):848–61. https://doi.org/10.2110/jsr.2009.092.

Loucks RG, Reed RM, Ruppel SC, Hammes U. Spectrum of pore types and networks in mudrocks and a descriptive classification for matrix-related mudrock pores. AAPG Bull. 2012;96(6):1071–98. https://doi.org/10.1306/08171111061.

Lowell S, Shields JE, Thomas MA, Thommes M. Characterization of porous solids and powders: surface area, pore size and density. Part Technol. 2004;16(9):1620.

Mastalerz M, He L, Melnichenko YB, Rupp JA. Porosity of coal and shale: insights from gas adsorption and SANS/USANS techniques. Energy Fuels. 2012;26(8):5109–20. https://doi.org/10.1021/ef300735t.

Pommer M, Milliken K. Pore types and pore-size distributions across thermal maturity, Eagle Ford Formation, southern Texas. AAPG Bull. 2015;99(09):1713–44. https://doi.org/10.1306/03051514151.

Sarkar P, Kumar A, Singh KH, Ghosh R, Singh TN. Pore system, microstructure and porosity characterization of Gondwana shale of Eastern India using laboratory experiment and watershed image segmentation algorithm. Mar Pet Geol. 2018;94:246–60. https://doi.org/10.1016/j.marpetgeo.2018.04.006.

Sing KSW, Everett DH, Haul RAW, Moscou L, Pierotti RA, Rouquerol J, et al. Reporting physisorption data for gas/solid systems with special reference to the determination of surface area and porosity. Pure Appl Chem. 1985;57:603–19.

Slatt RM, O'Brien NR. Pore types in the Barnett and Woodford gas shales: contribution to understanding gas storage and migration pathways in fine-grained rocks. AAPG Bull. 2011;95(12):2017–30. https://doi.org/10.1306/03301110145.

Song W, Yao B, Yao J, Li Y, Sun H, Yang Y, et al. Methane surface diffusion capacity in carbon-based capillary with application to organic-rich shale gas reservoir. Chem Eng J. 2018;352:644–54. https://doi.org/10.1016/j.cej.2018.07.050.

Sun M, Yu B, Hu Q, Yang R, Zhang Y, Li B, et al. Pore structure characterization of organic-rich Niutitang shale from China: small angle neutron scattering (SANS) study. Int J Coal Geol. 2018;186:115–25. https://doi.org/10.1016/j.coal.2017.12.006.

Sun F, Yao Y, Li G, Dong M. Transport behaviors of real gas mixture through nanopores of shale reservoir. J Pet Sci Eng. 2019;177:1134–41. https://doi.org/10.1016/j.petrol.2018.12.058.

Tian H, Pan L, Xiao X, Wilkins RWT, Meng Z, Huang B. A preliminary study on the pore characterization of Lower Silurian black shales in the Chuandong Thrust Fold Belt, southwestern China using low pressure N_2 adsorption and FE-SEM methods. Mar Pet Geol. 2013;48:8–19. https://doi.org/10.1016/j.marpetgeo.2013.07.008.

Veltzke T, Thöming J. An analytically predictive model for moderately rarefied gas flow. J Fluid Mech. 2012;698:406–22. https://doi.org/10.1017/jfm.2012.98.

Xiong J, Liu X, Liang L, Zeng Q. Adsorption of methane in organic-rich shale nanopores: an experimental and molecular simulation study. Fuel. 2017;200:299–315. https://doi.org/10.1016/j.fuel.2017.03.083.

Yang R, He S, Hu Q, Hu D, Zhang S, Yi J. Pore characterization and methane sorption capacity of over-mature organic-rich Wufeng and Longmaxi shales in the southeast Sichuan Basin, China. Mar Pet Geol. 2016;77:247–61. https://doi.org/10.1016/j.marpetgeo.2016.06.001.

Yao J, Sun H, Fan D, Wang C, Sun Z. Numerical simulation of gas transport mechanisms in tight shale gas reservoirs. Pet Sci. 2013;10(4):528–37. https://doi.org/10.1007/s12182-013-0304-3.

Yu H, Chen J, Zhu Y, Wang F, Wu H. Multiscale transport mechanism of shale gas in micro/nano-pores. Int J Heat Mass Transf. 2017;111:1172–80. https://doi.org/10.1016/j.ijheatmasstransfer.2017.04.050.

Yu H, Fan J, Chen J, Zhu Y, Wu H. Pressure-dependent transport characteristic of methane gas in slit nanopores. Int J Heat Mass Transf. 2018;123:657–67. https://doi.org/10.1016/j.ijheatmasstransfer.2018.03.003.

Yu H, Zhu Y, Jin X, Liu H, Wu H. Multiscale simulations of shale gas transport in micro/nano-porous shale matrix considering pore structure influence. J Nat Gas Sci Eng. 2019;64:28–40. https://doi.org/10.1016/j.jngse.2019.01.016.

Zhu H, Ju Y, Qi Y, Huang C, Zhang L. Impact of tectonism on pore type and pore structure evolution in organic-rich shale: implications for gas storage and migration pathways in naturally deformed rocks. Fuel. 2018;228:272–89. https://doi.org/10.1016/j.fuel.2018.04.137.